TESTING OF WIRE AND ARC ADDITIVELY MANUFACTURED TUBULAR SECTIONS

LEROY GARDNER[1], PINELOPI KYVELOU[2] and CRAIG BUCHANAN[3]

[1] *Civil & Environmental Engineering, Imperial College London, SW7 2AZ, UK*
E-mail: leroy.gardner@imperial.ac.uk
[2] *Civil & Environmental Engineering, Imperial College London, SW7 2AZ, UK*
E-mail: pinelopi.kyvelou11@imperial.ac.uk
[3] *Civil & Environmental Engineering, Imperial College London, SW7 2AZ, UK*
E-mail: craig.buchanan@imperial.ac.uk

Wire and arc additive manufacturing (WAAM) is a method of metal 3D printing that has the potential for significant impact in the construction industry. In order to gain insight into the structural behaviour of WAAM components, material and stub column testing has been undertaken and is presented herein. As-built and machined coupons were tested to investigate the influence of the as-built geometrical irregularity on the stress-strain characteristics while the material anisotropy was explored by testing coupons produced at 0°, 45° and 90° to the printing direction. Stub column tests on tubular sections were also conducted. Variation in the local slenderness of the tested specimens was considered by varying the cross-sectional proportions, allowing the influence of local buckling to be assessed while repeated tests enabled the variability in response to be evaluated. Advanced non-contact measurement techniques were employed to determine the geometric properties of the specimens, featuring 3D laser scanning, silicone casting and measurements based on the Archimedes' principle, while digital image correlation measurements were also used to provide detailed insight into the deformation characteristics of the specimens. Initial comparisons with existing design rules highlight the need for new design provisions that are specific to this form of manufacture.

Keywords: 3D printing, digital image correlation, laser scanning, tubular hollow sections, stub column testing, wire and arc additive manufacturing.

1 Introduction

Wire and arc additive manufacturing (WAAM) is a method of metal 3D printing in which wire feedstock is melted and selectively deposited on a substrate plate; the deposited material subsequently solidifies and the desired geometry is formed. WAAM has the potential for significant impact in the construction industry (Buchanan and Gardner 2019) since it can be used for the production of large-scale parts while allowing for high deposition rates, good structural integrity and reduced waste material compared to conventional manufacturing processes (Williams *et al*. 2015). Although other AM methods can achieve higher geometrical accuracy and complexity, WAAM can achieve reasonable lead times (Lockett *et al*. 2017) and uses mature welding technology and wire feedstock of low cost (Thompson *et al*. 2016).

The world's first large-scale demonstrator of WAAM for structural applications is the MX3D stainless steel 3D printed bridge, constructed by the Dutch company MX3D. The bridge has a mass of 4.5 tonnes, a span of 10.5 m and an average width of 2.5 m, while the total print time was about 1000 hours (Gardner *et al*. 2019). Being the first of its kind, having unfamiliar material properties and geometry beyond the coverage of existing design specifications, this

Proceedings of the 17th International Symposium on Tubular Structures.
Editors: X.D. Qian and Y.S. Choo

Published by Research Publishing, Singapore.
ISBN: 978-981-11-0745-0; doi:10.3850/978-981-11-0745-0_073-cd

novel structure requires extensive experimental and numerical research for its safety to be verified. Such fundamental research is also key for the wider adoption of the technology.

With this is mind, material and cross-sectional tests on 3D printed stainless steel circular (CHS) and square hollow sections (SHS) have been performed and the results are presented herein. The experiments were undertaken in the Structures Laboratory at Imperial College London, while the tested specimens were printed by MX3D employing the same feedstock material and printing parameters that were used for the bridge.

2 Material tests

In order to determine the stress-strain characteristics of the printed WAAM material, tensile material tests were undertaken. Dog-bone shaped coupons were extracted from plates with nominal thicknesses of 8 mm and 3.5 mm, printed using Grade 308LSi austenitic stainless steel wire. In order to investigate the inherent material anisotropy, coupons were extracted at 0°, 45° and 90° to the printing direction, as defined in Figure 1.

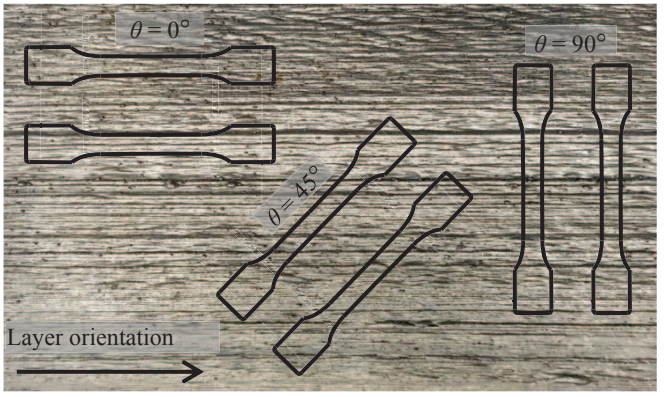

Figure 1. Orientation of tensile coupons extracted from WAAM plate

Owing to the undulating as-built surface of WAAM elements, material testing of the as-built coupons was expected to induce eccentricities and non-uniform deformations that would have a deleterious effect on the response. Hence, in order to allow for the pure underlying material properties to be determined, without this geometrical effect, machined coupons extracted at 0°, 45° and 90° to the printing direction were also tested; a comparison of the as-built and machined surface of a typical plate is shown in Figure 2(a) while the process of removing the surface undulations with an end mill is illustrated in Figure 2(b).

(a) (b)

Figure 2. (a) Comparison of as-built and machined surfaces and (b) machining of WAAM plate

The tensile coupon tests were conducted in compliance with EN ISO 6892-1 (2016). A four-camera LaVision digital image correlation (DIC) system was employed to provide accurate measurements of the surface strain field on both sides of the coupon along the parallel length. In total, 37 as-built and 12 machined coupons were tested.

A summary of the average material properties by printing direction (i.e. 0°, 45° and 90°) for the as-built and machined coupons is presented in Tables 1 and 2, respectively. In Tables 1 and 2, θ is the direction of testing relative to the layer direction as defined in Figure 1, t_{nom} is the nominal thickness of the coupon, E is the Young's modulus, $\sigma_{0.2}$ and $\sigma_{1.0}$ are the 0.2% and 1.0% proof stresses respectively, σ_u is the ultimate tensile stress, ε_u is the strain at the ultimate tensile stress and n, $n'_{0.2,1.0}$ and m are the strain hardening exponents of the two-stage Ramberg-Osgood material model (Ramberg and Osgood 1943, Hill 1944, Mirambell and Real 2000, Rasmussen 2003, Gardner and Ashraf 2006). Note that the material properties of the as-built material were determined based on the mean cross-sectional area over the parallel length of each coupon, as measured by 3D laser scanning.

Table 1. Average material properties of as-built coupons by direction of testing relative to the layer direction.

t_{nom} (mm)	θ (°)	E (MPa)	$\sigma_{0.2}$ (MPa)	$\sigma_{1.0}$ (MPa)	ε_u	σ_u (MPa)	n	$n'_{0.2,1.0}$	m
3.5	0	134700	340	368	0.271	560	18.0	1.9	2.2
	45	188700	348	395	0.255	574	10.4	2.4	2.3
	90	90700	263	322	0.116	451	7.0	2.6	2.6
8.0	0	135600	326	350	0.324	536	26.3	1.9	2.4
	45	201200	351	392	0.255	560	12.0	2.3	2.3
	90	107200	270	324	0.103	422	6.0	2.7	2.5

Table 2. Average material properties of machined coupons by direction of testing relative to the layer direction.

θ (°)	E (MPa)	$\sigma_{0.2}$ (MPa)	$\sigma_{1.0}$ (MPa)	ε_u	σ_u (MPa)	n	$n'_{0.2,1.0}$	m
0	143900	358	383	0.309	577	17.5	1.7	2.4
45	215400	403	432	0.364	622	15.5	2.0	2.3
90	138400	333	376	0.296	550	7.4	2.3	2.7

The results highlight the anisotropic behaviour of the printed material, with the 45° coupons exhibiting the highest values of Young's modulus and strength in both the machined and as-built conditions. As expected, the as-built specimens exhibited lower values of Young's modulus and strength compared to the machined specimens, with the 90° coupons showing the most severe reductions (up to about 35%, 20% and 21% reductions in E, $\sigma_{0.2}$ and σ_u, respectively). Hence, it can be inferred that the irregular geometry has a detrimental effect on the mechanical properties of the WAAM material, being more prominent for loading acting perpendicular to the layer orientation.

3 Stub column tests

Compression tests on WAAM CHS and SHS stub columns were conducted to investigate their compressive structural response and load carrying capacity. Simple geometries (i.e. circular and square) were chosen deliberately for the stub column test specimens to enable the influence of the production process alone on the exhibited structural response, in comparison to traditionally

manufactured tubular sections, to be isolated. Variation in the local cross-section slenderness of the tested specimens was considered by varying the cross-sectional proportions, allowing the influence of local buckling to be assessed, while repeated tests enabled the variability in response to be evaluated; 10 CHS and 8 SHS stub columns were tested in total.

Following their fabrication, the stub columns were cut to specified lengths chosen to be long enough to include a representative distribution of residual stresses and geometric imperfections, yet short enough to prevent overall flexural buckling (Ziemian 2010). Both ends of the stub columns were machined to be flat and parallel, while their full surface was sandblasted with glass beads for the specimens shorter than 1000 mm and jet pressure washed for longer specimens, to remove any welding soot from the WAAM process.

The adopted labelling system for the test specimens begins with the letter C for CHS and S for SHS; this is followed by the cross-sectional dimensions in mm (in the form diameter×thickness for the CHS and width×depth×thickness for the SHS), followed by the nominal length in mm and the letter 'F' indicating fixed end conditions; a specimen ending with 'R' is a repeat test.

3.1 *Geometrical measurements*

Measuring the geometry of the stub columns proved to be challenging due to the inherent surface undulations and wall thickness variation arising as a result of the WAAM fabrication process. A number of sophisticated measurement techniques were employed to determine the as-built geometric properties of the specimens, featuring 3D laser scanning, silicone casting and measurements based on Archimedes' principle.

The water displacement method, which is based on Archimedes' physical law of buoyancy and is frequently employed to determine porosity in concrete elements (Park and Tia 2004, Ibrahim *et al*. 2014), was utilised for the determination of the average cross-sectional areas of the examined stub columns. Each specimen was hung using chains from weighing scales and its mass was measured both when in air and when submerged in a water bath, subtracting the mass of the chain; the employed setup is illustrated in Figure 3(a). The mean cross-sectional area of the specimens A_{Arch}, reported in Table 3, was hence determined by dividing the resulting volume V by the member length L, which had been measured using calipers.

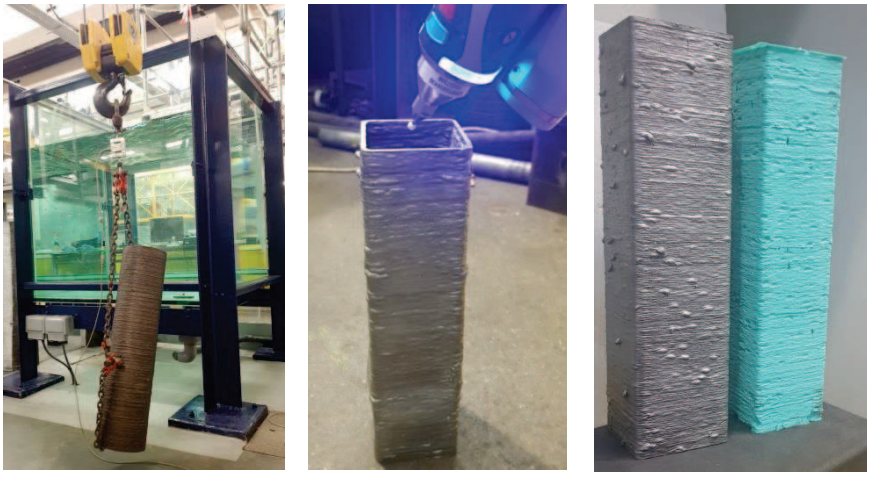

(a) Archimedes' measurements (b) Laser scanning (c) Silicone cast of inner profile

Figure 3. Employed methods for geometrical measurements of WAAM stub columns

In order to obtain a more accurate and detailed replication of the external and internal surfaces of all specimens, laser scanning was also employed. A FARO ScanARM, capable of capturing up to 600,000 points per second to an accuracy of 0.1 mm, was used to scan and digitally reproduce all specimens. Although full scans of the outer surface of the specimens were taken, the physical size of the head of the laser scan arm prevented direct scanning of the inner surface profile – see Figure 3(b). Hence, silicone casting was employed to create a replica of the internal surface of the specimens, as shown in Figure 3(c). The outer and inner scans of the as-built geometries were then successfully merged and converted into full 3D CAD models, with polygonal meshes, using Geomagic Wrap (2017). The CAD models were then imported into Rhinoceros 3D (2017) for their geometrical properties to be determined. The mean cross-sectional areas of the specimens A_{lsr} as determined by laser scanning are presented in Table 3. Good agreement was found between the cross-sectional areas A_{Arch} and A_{lsr}, which were consistently within 2%, providing confidence in the employed laser scanning technique.

3.2 *Test setup*

The experimental layout adopted for the CHS stub column tests is presented in Figure 4. The load was applied through an Instron 3500kN-SPL testing machine while a self-locking spherical head was used to ensure full contact between the stub column ends and end platens. Three equally spaced linear variable displacement transducers (LVDTs) were used to measure the vertical movement of the top platen of the testing machine while a load cell within the machine measured the applied load. A two camera LaVision DIC system was also used, allowing surface deformations and strains fields to be recorded for roughly one third of the surface area of specimen. The SHS setup was similar to the CHS setup, with four equally spaced LVDTs used to measure the top platen movement and with the DIC system monitoring one flat face of the specimen. The load was applied using displacement control, at a rate of 0.2 mm/min for the CHS and 0.5 mm/min for the SHS specimens, and was recorded simultaneously with the image acquisition through an analogue-to-digital (A/D) convertor. The tests were continued beyond the ultimate load and the post-ultimate response was also recorded.

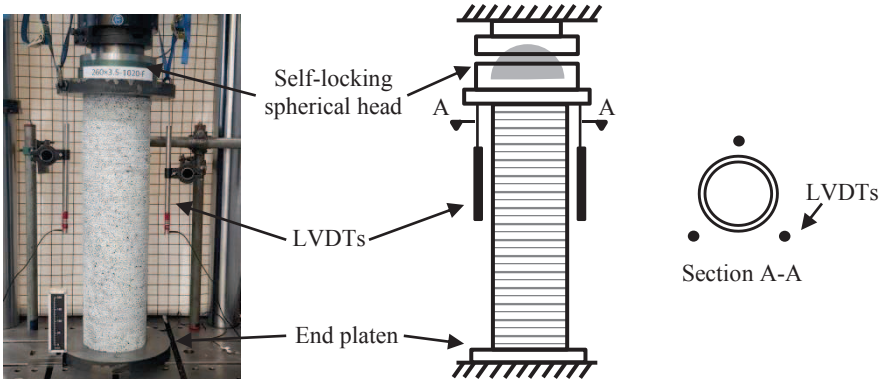

Figure 4. Test setup for CHS stub columns

3.3 *Results*

The deformed shapes of the stub columns, shown in Figure 5, although akin to the classical local buckling modes associated with CHS and SHS, were clearly influenced by the initial imperfections inherent to the WAAM process (i.e. the surface undulations). The marked

variation in behavior and capacity between repeat specimens (see Tables 3 and 4) reflects the greater geometric variability associated with WAAM cross-sections relative to conventional sections.

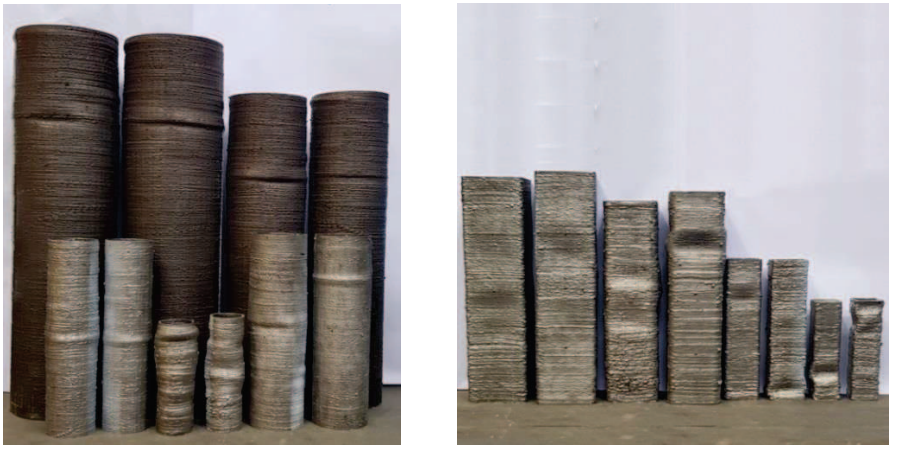

(a) CHS (b) SHS

Figure 5. Deformed shapes of tested (a) CHS and (b) SHS stub columns

A summary of the obtained results for the CHS and SHS specimens is given in Tables 3 and 4 respectively, where N_u is the ultimate axial load and δ_u is the column end shortening at N_u as calculated from the DIC data. Note that the results yielded by the LVDT and DIC measurements were almost identical. The cross-sectional classes according to EN 1993-1-4 (2015), local slendernesses, $D/(t\varepsilon^2)$ and $c/t\varepsilon$ for the CHS and SHS respectively, where D is the mean diameter of the CHS, c is the mean flat width of the faces of the SHS, t is the mean thickness and $\varepsilon=[(235/\sigma_{0.2})(E/210000)]^{0.5}$ with $\sigma_{0.2}$ and E based on the measured properties from the machined 90° coupons as given in Table 2, and ultimate load normalized by the yield load, N_u/N_y with the yield load calculated as $N_y = A_{lsr}\,\sigma_{0.2}$ based on the mean area recorded from the laser scan, are also reported in Tables 3 and 4.

Table 3. CHS stub column test results.

Specimen	A_{Arch} (mm^2)	A_{lsr} (mm^2)	A_{Arch} / A_{lsr}	N_u (kN)	δ_u (mm)	EC3 class	$D/(t\varepsilon^2)$	N_u/ N_y	N_u/ $N_{u,EC3}$
C-105×8-355-F	2108	2111	1.00	942.8	37.78	1	32.0	1.34	1.34
C-105×8-355-FR	1976	2010	0.98	728.9	21.08	1	32.5	1.09	1.09
C-140×3.5-560-F	1589	1643	0.97	482.1	6.22	3	76.9	0.88	0.88
C-140×3.5-560-FR	1691	1629	1.04	442.5	4.48	3	77.7	0.82	0.82
C-170×3.5-580-F	1928	1936	1.00	530.8	4.33	4	98.6	0.82	0.86
C-170×3.5-580-FR	1972	1930	1.02	563.8	4.55	4	102.5	0.88	0.94
C-260×3.5-1020-F	3056	3069	1.00	664.3	4.05	4	144.6	0.65	0.82
C-260×3.5-1020-FR	3064	3101	0.99	692.7	4.71	4	142.6	0.67	0.84
C-320×3.5-1180-F	3742	3910	0.96	849.2	5.16	4	172.1	0.65	0.90
C-320×3.5-1180-FR	3707	3783	0.98	858.0	5.63	4	177.9	0.68	0.96

Furthermore, comparisons against the resistance predictions $N_{u,EC3}$ determined according to EN 1993-1-4 (2015) and also against the capacities of conventional and powder-bed fusion (PBF) manufactured (Buchanan *et al.* 2017) stainless steel CHS and SHS members are presented in Figure 6. The results show that the only design resistance predictions that are on the safe side

are for the stockier sections where the benefit of strain hardening (which is not captured in the EC3 calculations) outweighs the negative influence of the most severe imperfections, while the resistances of the more slender sections are overpredicted. This reflects primarily the greater geometric variability associated with WAAM cross-sections relative to hot-rolled and cold-formed sections and highlights the need for design provisions that are specific to this form of manufacture.

Table 4. SHS stub column test results.

Specimen	A_{Arch} (mm^2)	A_{lsr} (mm^2)	A_{Arch} / A_{lsr}	N_u (kN)	δ_u (mm)	EC3 class	$c/(t\varepsilon)$	N_u / N_y	N_u/ $N_{u,EC3}$
S-60×60×3.5-240-F	888	902	0.98	277.5	5.84	1	18.8	0.92	0.92
S-60×60×3.5-240-FR	839	847	0.99	250.6	5.74	1	20.2	0.89	0.89
S-80×80×3.5-320-F	1192	1222	0.98	353.0	3.69	1	26.1	0.87	0.87
S-80×80×3.5-320-FR	1153	1184	0.97	314.1	3.25	1	26.7	0.80	0.80
S-120×120×8-450-F	2877	2898	0.99	993.2	8.86	1	21.7	1.03	1.03
S-120×120×8-450-FR	2701	2759	0.98	841.1	6.64	1	22.9	0.91	0.91
S-130×130×3.5-500-F	1841	1875	0.98	437.4	2.23	4	46.8	0.70	0.85
S-130×130×3.5-500-FR	1829	1877	0.97	414.8	1.87	4	46.5	0.66	0.80

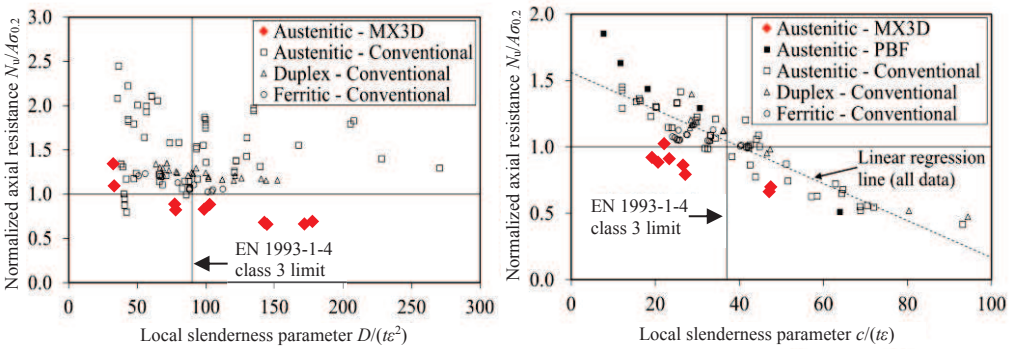

(a) CHS (b) SHS

Figure 6. Comparison of design predictions for 3D printed sections with EC3 slenderness limits and test data on conventionally manufactured stub columns

4 Conclusions

An experimental study into the material and cross-sectional properties of WAAM stainless steel elements has been presented. The research was carried out to gain further insight into the structural behaviour of 3D printed stainless steel members and, also, to complement the safety verification of the world's first metal 3D printed bridge.

The conducted material tests revealed substantial anisotropy, with the direction of loading relative to the printing orientation having a strong influence on the stress-strain characteristics. The 45° coupons exhibited the highest values of Young's modulus and strength. The irregular geometry associated with the WAAM process resulted in further reductions in the obtained material properties for the as-built material.

Compression tests were performed on 10 CHS and 8 SHS stub columns, covering a wide range of local slendernesses, aiming at the determination of their cross-sectional behavior under compression. Sophisticated non-contact measurement techniques were employed to determine the as-built geometric properties of the specimens, featuring 3D laser scanning, silicone casting

and measurements based on Archimedes' principle, while digital image correlation measurements were also used to provide detailed insight into the deformation characteristics of the test specimens. Initial comparisons of the test results with existing design rules highlighted the need for new design provisions that are specific to this form of manufacture.

Acknowledgments

The research presented in this paper was possible thanks to funding and support from Engineering and Physical Sciences Research Council (EPSRC) and the Data Centric Engineering programme at the Alan Turing Institute (ATI). The authors would also like to acknowledge the contributions of Angeline Tan, Harry Slack, Qianwen Han, Gordon Herbert and Paul Crudge in the experimental programme.

References

Buchanan, C. and Gardner, L., Metal 3D printing in construction: a review of methods, research, applications, opportunities and challenges, *Engineering Structures*, 180, 332-348, 2019.

Buchanan, C., Matilainen, V.P., Salminen, A. and Gardner, L., Structural performance of additive manufactured metallic material and cross-sections, *Journal of Constructional Steel Research*, 136, 35-48, 2017.

EN 1993-1-4, *Eurocode 3 - Design of Steel Structures - Part 1–4: General Rules - Supplementary Rules for Stainless Steels*, European Committee for Standardization (CEN), Brussels, 2015.

EN ISO 6892-1, *Metallic materials - Tensile testing – Part 1: Method of test at room temperature*, Brussels, European Committee for Standardization (CEN), Brussels, 2016.

Gardner, L. and Ashraf, M., Structural design for non-linear metallic materials, *Engineering Structures*, 28 (6), 926-934, 2006.

Gardner, L., Buchanan, C., Kyvelou P. and Herbert, G., Testing and verification of the world's first metal 3D printed bridge, in *Proceedings of the 9th International Conference on Steel and Aluminium Structures (ICSAS19)*, 3-5 July, Bradford, UK, 2019.

Geomagic Wrap, 3D Systems Inc, 2017.

Hill, H., Determination of stress-strain relations from the offset yield strength values, *Technical Note No. 927, National Advisory Committee for Aeronautics*, Washington, D.C., USA, 1944.

Ibrahim, A., Mahmoud, E., Yamin, M. and Patibandla, V.C., Experimental study on Portland cement pervious concrete mechanical and hydrological properties, *Construction and Building Materials*, 50, 524-529, 2014.

Lockett, H., Ding, J., Williams, S. and Martina, F., Design for Wire + Arc Additive Manufacture: design rules and build orientation selection, *Journal for Engineering Design*, 28 (7-9), 568-598, 2017.

Park, S.B. and Tia, M., An experimental study on the water-purification properties of porous concrete, *Cement and Concrete Research*, 34, 177-184, 2004.

Ramberg, W. and Osgood, W.R., Description of stress-strain curves by three parameters, *Technical Note No. 902, National Advisory Committee for Aeronautics*, Washington, D.C., USA, 1943.

Rasmussen, K. J. R., Full-range stress-strain curves for stainless steel alloys, *Journal of Constructional Steel Research*, 59 (1), 47-61, 2003.

Rhinoceros 3D, Robert McNeel & Associates, 2017.

Thompson, M.K., Moroni, G., Vaneker, T., Fadel, G., Campbell, R.I., Gibson, I., Bernard, A., Schulz, J., Graf, P., Ahuja, B. and Martina, F., Design for Additive Manufacturing: Trends, opportunities, considerations, and constraints, *CIRP Annals – Manufacturing Technology*, 65 (2), 737-760,2016.

Williams, S.W., Martina, F., Addison, A.C., Ding, J., Pardal, G. and Colegrove, P.A., Wire + Arc Additive Manufacturing, *Materials Science and Technology*, 32 (7), 641-647, 2015.

Ziemian, R.D., *Guide to Stability Design Criteria for Metal Structures*, 6th edition, John Wiley & Sons, Inc, New York, 2010.